Available online at www.sciencedirect.com

SciVerse ScienceDirect

Scripta Materialia xxx (2012) xxx–xxx

Scripta MATERIALIA

www.elsevier.com/locate/scriptamat

Hydrogen-induced cracking at grain and twin boundaries in an Fe–Mn–C austenitic steel

Motomichi Koyama,[a,b,*] Eiji Akiyama,[b] Takahiro Sawaguchi,[b] Dierk Raabe[c] and Kaneaki Tsuzaki[a,b]

[a] *Doctoral Program in Materials Science and Engineering, University of Tsukuba, 1-2-1 Sengen, Tsukuba, Ibaraki 305-0047, Japan*
[b] *National Institute for Materials Science, 1-2-1 Sengen, Tsukuba, Ibaraki 305-0047, Japan*
[c] *Max-Planck-Institut für Eisenforschung, Max-Planck-Str. 1, Düsseldorf 40237, Germany*

Received 25 November 2011; revised 15 December 2011; accepted 15 December 2011

Hydrogen embrittlement was observed in an Fe–18Mn–1.2C (wt.%) steel. The tensile ductility was drastically reduced by hydrogen charging during tensile testing. The fracture mode was mainly intergranular fracture, though transgranular fracture was also partially observed. The transgranular fracture occurred parallel to the primary and secondary deformation twin boundaries, as confirmed by electron backscattering diffraction analysis and orientation-optimized electron channeling contrast imaging. The microstructural observations indicate that cracks are initiated at grain boundaries and twin boundaries.

Keywords: Austenitic steel; Tension test; Electron backscattering; Hydrogen embrittlement; Twinning

High-Mn austenitic steels are used as Hadfield [1–3], shape memory [4,5], damping [6], seismic-resistant [7], transformation-induced plasticity [8–10] and twinning-induced plasticity (TWIP) steels [9–13]. The excellent mechanical properties of this alloy group mainly derive from displacive mechanisms, such as martensitic transformation and deformation twinning.

High-Mn steels can undergo premature fracture under a variety of microstructural conditions, such as under stress concentrations at the tips of ε-martensite plates (hexagonal close-packed phase) [14] or face-centered cubic deformation twins [15] interacting with grain and phase boundaries; at cementite particles [16]; in Mn-enriched segregation zones at grain boundaries [17]; and in interaction zones between annealing twin boundaries and ε-martensite [18]. Other, more globally observed, phenomena include failure due to stress corrosion cracking [19] and hydrogen embrittlement [20–24]. In particular, hydrogen embrittlement has recently become a point of major interest due to the use of TWIP steels in automotive and safety-relevant parts for a reduced-carbon industrial infrastructure [20,25].

Key factors of hydrogen embrittlement in high-Mn steels are phase stability, residual stress and the cohesive energy of grain boundaries. In order to rule out the influence of insufficient austenite stability on embrittlement, we chose here an alloy composition with large amounts of Mn and C, namely, Fe–18Mn–1.2 C (wt.%). The steel shows about 80% uniform elongation and 1.1 GPa tensile strength [26], mainly due to deformation twinning and its interaction with the dislocation substructure. This combination of elongation and strength provides an excellent property profile.

The steel was prepared by induction melting. The ingot was forged and hot rolled at 1273 K. It was then solution treated at 1273 K for 3600 s under an argon atmosphere and subsequently water quenched to suppress carbide formation. The chemical composition of the steel is shown in Table 1. The average grain size was 46 μm, not counting annealing twin boundaries. Tensile specimens with gauge dimensions of 4 mm × 0.5 mm × 10 mm and grip sections at both ends were cut by spark erosion.

Tensile tests were conducted at ambient temperature around 294 K and at an initial strain rate of $5.1 \times 10^{-5}\ s^{-1}$ along the rolling direction (RD) using an Instron machine. Total elongations were determined by measuring the gauge length before and after the tests.

* Corresponding author at: National Institute for Materials Science, 1-2-1 Sengen, Tsukuba, Ibaraki 305-0047, Japan. Tel.: +81 29 859 2000; fax: +81 29 859 2101.; e-mail: KOYAMA.Motomichi@nims.go.jp

1359-6462/$ - see front matter © 2011 Acta Materialia Inc. Published by Elsevier Ltd. All rights reserved.
doi:10.1016/j.scriptamat.2011.12.015

Table 1. Chemical composition in the present steel.

Steel (wt.%)	Mn	Si	C	Fe
Fe–18Mn–1.2C	18.0	0.003	1.15	Bal.

All stress–strain curves obtained from the load–displacement data were fitted to the total elongations that were evaluated from the change in the gauge length. Hydrogen was introduced into the specimens during the tensile tests by electrochemical charging in a 3% NaCl aqueous solution containing 3 g l^{-1} of NH_4SCN at a current density of 10 A m^{-2}. A platinum wire was used as the counter electrode. The solution was continuously added to cover the gauge part of the sample during the tensile tests. Hydrogen charging during tensile testing effectively introduced hydrogen into the samples via diffusion, as well as through the motion of hydrogen-decorated dislocations [27,28].

Microstructure observations were performed by secondary electron imaging (SEI), electron backscattering diffraction and orientation-optimized electron channeling contrast imaging (ECCI) to observe cracks and deformation twins. Orientation-optimized ECCI has recently been used to reveal deformation twins and complex dislocation substructures in TWIP steels [12,29,30]. Specimens for scanning electron microscopic observation were prepared by mechanical polishing with colloidal silica long enough to remove the layers affected by polishing with coarser particles.

Hydrogen uptake was measured by thermal desorption analysis (TDA) from room temperature to 550 K. TDA was conducted immediately after the tensile test. The time that elapsed between the end of the tensile test and the TDA analysis was less than 20 min. The heating rate was 100 K h^{-1}. The diffusible hydrogen content was determined by measuring cumulative desorbed hydrogen from room temperature to 473 K. The diffusible hydrogen is defined as the amount of hydrogen that diffuses at room temperature. It has been reported to play a key role in hydrogen embrittlement [31].

Figure 1a shows two groups of engineering stress–strain curves, one with and one without hydrogen charging. The fracture stress and elongation values were reduced significantly by the hydrogen charging. Hydrogen can have multiple effects in that context. It is known that hydrogen entry into austenitic steels reduces their stacking fault energy [32,33]. This effect promotes ε-martensitic transformation [34,35] and deformation twinning [36,37]. However, the immediate effect of hydrogen charging on the deformation microstructure seems to be small in the present steel, because both the yield strength and the work hardening behavior, which are typically strongly affected by the microstructure [10,38], hardly changed upon hydrogen charging in the present case, as shown in Figure 1a. Figure 1b shows the hydrogen desorption rate curves of the steel with and without hydrogen charging, demonstrating that a significant amount of hydrogen was indeed introduced into the steels by the present method: the diffusible hydrogen content, H_D, within the steel with and without hydrogen charging was 1.10 and 0.05 wt. ppm, respectively. The diffusible hydrogen was reported to be potentially trapped at dislocations, in the matrix (here preferentially at vacancies) and at grain boundaries in a TWIP steel [39]. Additionally, twin boundaries can also act as trapping sites for hydrogen [39]. The degree of degradation in the tensile ductility is similar to our previous results obtained for an Fe–18Mn–0.6C TWIP steel [24].

Figure 2a shows a fractograph of the hydrogen-charged Fe–18Mn–1.2C steel. The central region that the hydrogen did not reach during charging revealed a ductile fracture surface. In contrast, a brittle fracture surface was observed from the surface down to about 150 μm. The facet size of the brittle fracture areas is about 50 μm, which corresponds to the grain size, indicating that intergranular fracture was caused by hydrogen charging. Intergranular fracture caused by hydrogen entry has previously been reported in high-Mn steels [21,24,40]. However, the present intergranular fracture surface also includes another type of crack. Figure 2b shows a magnified image of Figure 2a. The intergranularly fractured parts are further cracked, as indicated by the arrows. All the cracks in a group are parallel to each other. In addition, the distance between the subcracks in the intergranularly fractured part is about 3 μm, which is much shorter than the grain size, indicating that the cracks were induced along a specific microstructure within each grain.

Figure 3a and b shows an SEI micrograph and an RD-inverse pole figure (IPF) map of a polished surface showing a crack. The RD-IPF map is superimposed on the detector signal image. The crystal orientations across the main crack are completely different, indicating that the main crack was induced along grain boundaries. The SEI micrograph in Figure 3c is the of the area contained within the square in Figure 3a. Subcracks were observed near the main crack, as shown in Figure 3c. Figure 3d and e shows image quality (IQ) and higher resolution RD-IPF maps taken at a step size of 50 nm. The plate-like contrasts in the IQ map stem from overlaps of two Kikuchi patterns [41], indicating that plate-like products such as martensite or deformation twins were formed. The red lines in Figure 3e indicate twin boundaries.[1] The combination of IQ and RD-IPF maps hence enables us to identify primary deformation twins.

An orientation-optimized ECCI image is shown in Figure 3f. Orientation-optimized ECCI can provide quantitative information about dislocation structures and nanoscale deformation twins with a wide field of view [12,29,30]. In addition to the primary twins on $(1\,1\,\bar{1})$ planes with bright contrast, the ECCI image also reveals very thin plates, as indicated by the black arrows. The thin plates are secondary deformation twins or stacking faults acting as nuclei for twins on $(1\,\bar{1}\,1)$ planes. This image thus shows that the cracks propagate parallel to the secondary twinning plane and partially along the primary deformation twin boundaries, as indicated by the red arrows in Figure 3f.

[1] For interpretation of color in Figure 3, the reader is referred to the web version of this article.

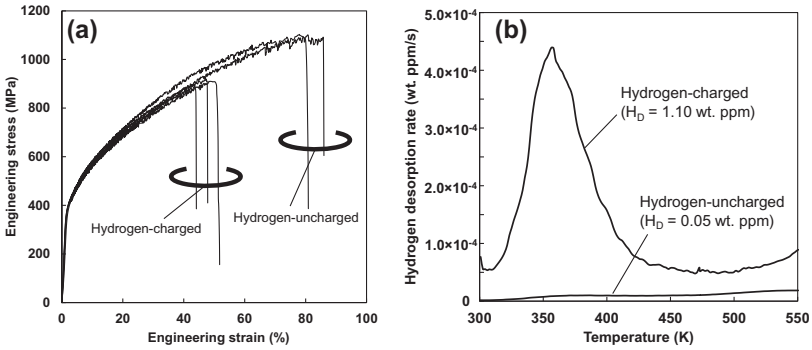

Figure 1. (a) Engineering stress–strain curves and (b) hydrogen desorption rate curves in the steel with and without hydrogen charging.

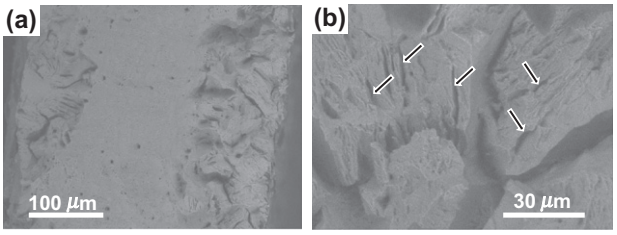

Figure 2. Fractographs with low and high magnifications in the hydrogen-charged steel.

Since the cracks are initiated in the grain and propagate parallel to primary and secondary twin boundaries, the interception of secondary deformation twins at the primary twin boundaries seems to cause transgranular fracture. This fracture is thus the cause of the parallel cracks shown in Figure 2b. However, initially, primary deformation twins are intercepted by grain boundaries (Fig. 4a), probably causing intergranular fracture when the cohesive energy at the grain boundaries is reduced by hydrogen loading (Fig. 4b). Thus, the primary fracture mode is intergranular fracture, followed by twin–twin interactions, which cause partial transgranular fracture (Fig. 4c) in the present steel. The propagation path of the cracks that were initiated by the twin–twin interaction was observed to follow primary and secondary deformation twin boundaries. The crack propagation path is determined by the crystallographic orientation relationship between the tensile direction and the normal to the twin boundary.

In summary, tensile tests in conjunction with hydrogen charging and detailed fracture and microstructure analyses was conducted. The tensile strength and ductility were both severely reduced by hydrogen charging (about 20% reduced strength and about 40% reduced ductility). Two kinds of cracking were observed, namely, intergranular fracture and transgranular fracture along twin boundaries. The present results suggest that the important factors in hydrogen embrittlement of Fe–Mn–C austenitic steels are the reduction in cohesive energy at grain boundaries and twin boundaries, and the stress concentrations caused by the interception of deformation twins. The fact that cracks were initiated

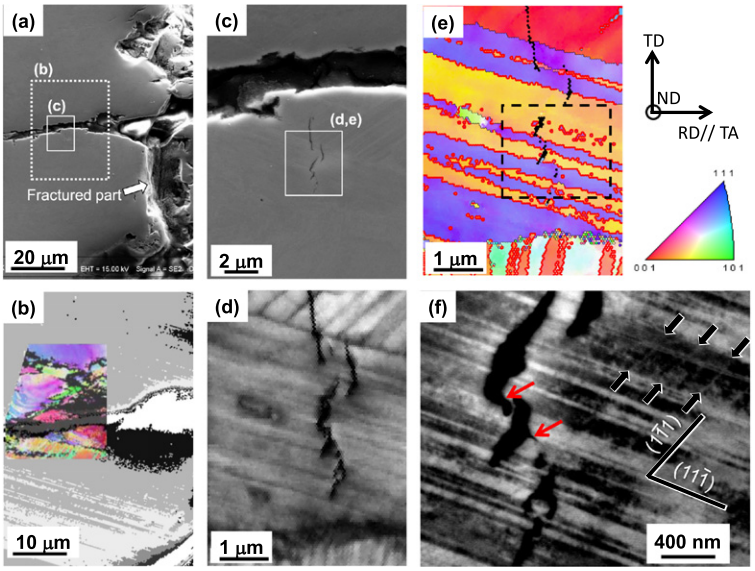

Figure 3. A set of micrographs near the crack. (a) SEI micrograph. (b) RD-IPF map with a beam step size of 300 nm superimposed on the detector signal image. (c) Magnified image of the area within the white lines in (a). (d and e) IQ and RD-IPF maps with a step size of 50 nm corresponding to the area within the white lines in (c). (f) Orientation-optimized ECCI micrograph corresponding to the area within the black broken lines in (e). ND, normal direction; TD, transverse direction; TA, tensile axis.

Please cite this article in press as: M. Koyama et al., Scripta Mater. (2012), doi:10.1016/j.scriptamat.2011.12.015

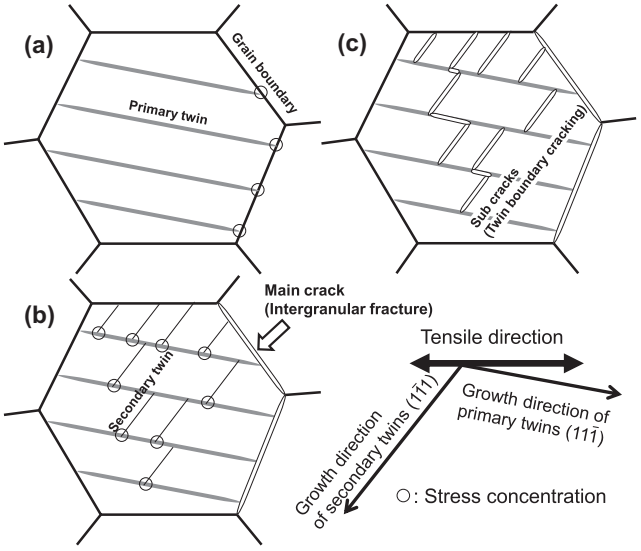

Figure 4. Schematics for the cracking. (a) Stress concentration caused by primary twins at grain boundaries. (b) Formation of main cracks (intergranular fracture), and stress concentration caused by secondary twins at primary twin boundaries. (c) Formation of sub cracks (twin boundary cracking).

from twin boundaries is crucially important, because deformation twinning is essentially required to achieve the superior mechanical properties of TWIP steels.

M.K. acknowledges the Research Fellowship of the Japan Society for the Promotion of Science for Young Scientists. The Materials Manufacturing and Engineering Station and Materials Analysis Station at the National Institute for Materials Science supported this work through the production of the samples and carrying out the analysis of the chemical compositions. The microstructural observations were supported by Ms. N. Elhami and Mr. T. Jäpel at Max-Planck-Institut für Eisenforschung.

[1] R.A. Hadfield, J. Forrest, Manganese Steel: Manganese in its Application to Metallurgy, Some Newly-Discovered Properties of Iron and Manganese, Kessinger Publishing, Kila, MT, 1888.
[2] Y.N. Dastur, W.C. Leslie, Metall. Trans. A 12A (1981) 749.
[3] P.H. Adler, G.B. Olson, W.S. Owen, Metall. Trans. A 17A (1986) 1725.
[4] A. Sato, E. Chishima, K. Soma, T. Mori, Acta Metall. 30 (1982) 1177.
[5] M. Murakami, H. Otsuka, H.G. Suzuki, S. Matsuda, Proc. ICOMAT (1986) 985.
[6] S.-H. Baik, J.-C. Kim, K.-K. Jee, M.-C. Shin, C.-S. Choi, ISIJ Int. 37 (1997) 519.
[7] T. Sawaguchi, L.-G. Bujoreanu, T. Kikuchi, K. Ogawa, M. Koyama, M. Murakami, Scripta Mater. 59 (2008) 826.
[8] I. Tamura, Met. Sci. 16 (1982) 245.
[9] O. Grässel, G. Frommeyer, Mater. Sci. Technol. 14 (1998) 1213.
[10] L. Remy, A. Pineau, Mater. Sci. Eng. 28 (1977) 99.
[11] O. Bouaziz, S. Allain, C. Scott, Scripta Mater. 58 (2008) 484.
[12] I. Gutierrez-Urrutia, D. Raabe, Acta Mater. 59 (2011) 6449.
[13] C. Curtze, V.-K. Kuokkala, Acta Mater. 58 (2010) 5129.
[14] K. Sipos, L. Remy, A. Pineau, Metal. Trans. A 7A (1976) 857.
[15] H. Suto, B.S. Chun, Tech. Report, Tohoku University, vol. 44, 1979, p. 317.
[16] A. Goldberg, O.A. Ruano, O.D. Sherby, Mater. Sci. Eng. A 150 (1992) 187.
[17] Y. Tomota, M. Strum, J.W. Morris, Jr. Metal. Trans. A 18A (1987) 1073.
[18] M. Koyama, T. Sawaguchi, K. Tsuzaki, ISIJ Int. 52 (2012) 168.
[19] H.C. Lin, K.M. Lin, C.S. Lin, T.M. Ouyang, Corros. Sci. 44 (2002) 2013.
[20] O. Kwon, in: Proceedings of HMnS, 2011 (CD-ROM).
[21] K.-G. Chin, C.-Y. Kang, S.Y. Sin, S. Hong, S. Lee, H.-S. Kim, K.-H. Kim, N.J. Kim, Mater. Sci. Eng. A 528 (2011) 2922.
[22] B.C. De Cooman, K.-G. Chin, J. Kim, in: M. Chiaberge (Ed.), New Trends and Developments in Automotive System Engineering, InTech, Rijeka, 2011.
[23] R.T. van Tol, L. Zhao, J. Sietsma, in: Proceedings of HMnS, 2011 (CD-ROM).
[24] M. Koyama, E. Akiyama, K. Tsuzaki, Corros. Sci. 54 (2012) 1.
[25] C. Scott, S. Allain, M. Faral, N. guelton, Rev. Metal. Cah. Inf. Tech. 103 (2006) 293.
[26] T. Sasaki, K. Watanabe, K. Nohara, Y. Ono, N. Kondo, T. Sasaki, S. Sato, I. Ichise, Kawasaki Steel Technical Report, vol. 13, 1981, p. 62.
[27] G.S. Frankel, R.M. Latanision, Metal. Trans. A 17A (1986) 869.
[28] J.K. Tien, A.W. Thompson, I.M. Bernstein, R.J. Richards, Metal. Trans. A 7A (1976) 821.
[29] I. Gutierrez-Urrutia, S. Zaefferer, D. Raabe, Scripta Mater. 61 (2009) 737.
[30] I. Gutierrez-Urrutia, S. Zaefferer, D. Raabe, Mater. Sci. Eng. A 527 (2010) 3552.
[31] K. Takai, R. Watanuki, ISIJ Int. 43 (2003) 520.
[32] M.B. Whiteman, A.R. Troiano, Phys. Status. Solidi 7 (1964) K109.
[33] A.E. Pontini, J.D. Hermida, Scripta Mater. 37 (1997) 1831.
[34] P. Rozenak, D. Eliezer, Acta Metall. 35 (1987) 2329.
[35] N. Narita, C.J. Altstetter, H.K. Birnbaum, Metal. Trans. A 13A (1982) 1355.
[36] J.M. Rigsbee, J. Mater. Sci. 12 (1977) 406.
[37] E.G. Astafurova, G.G. Zakharova, H.J. Maier, Scripta Mater. 63 (2010) 1189.
[38] M. Koyama, T. Sawaguchi, T. Lee, C.S. Lee, K. Tsuzaki, Mater. Sci. Eng. A 528 (2011) 7310.
[39] K.H. So, J.S. Kim, Y.S. Chun, K.-T. Park, Y.-K. Lee, C.S. Lee, ISIJ Int. 49 (2009) 1952.
[40] S.C. Mittal, R.C. Prasad, M.B. Deshmukh, ISIJ Int. 34 (1994) 211.
[41] D. Barbier, N. Gey, N. Bozzolo, A. Allain, M. Humbert, J. Microsc. 235 (2009) 6.